LAWRENCE
LIVERMORE
NATIONAL
LABORATORY

LLNL-JRNL-821645

Scalable gas diffusion electrode fabrication for electrochemical CO2 reduction using physical vapor deposition methods

E. Jeng , Z. Qi, A. R. Kashi, S. Hunegnaw, Z. Huo , J. S. Miller, L. B. Bayu-Aji, B. H. Ko, H. Shin, S. Ma, K. P. Kuhl, F. Jiao, J. Biener

April 16, 2021

ACS Applied Materials and Interfaces

Disclaimer

Scalable Gas Diffusion Electrode Fabrication for Electrochemical CO_2 Reduction using Physical Vapor Deposition Methods

Emily Jeng[a†], Zhen Qi[b†], Ajay R. Kashi[c], Sara Hunegnaw[c], Ziyang Huo[c], John S. Miller[b], Leonardus B. Bayu-Aji[b], Byung Hee Ko[a], Haeun Shin[a], Sichao Ma[c], Kendra P. Kuhl[c], Feng Jiao[a], and Juergen Biener[b]**

a Center for Catalytic Science & Technology, Department of Chemical and Biomolecular Engineering, University of Delaware, Newark, DE, 19716, USA

b Materials Science Division, Physical and Life Sciences Directorate, Lawrence Livermore National Laboratory, 7000 East Ave., Livermore, CA, 94550, USA

c Twelve Incorporated (formerly Opus 12 Incorporated), 614 Bancroft Way, Berkeley, CA, 94710 USA

Keywords: electrochemical CO_2 reduction, physical vapor deposition, catalyst morphology, copper catalyst, energy efficiency

Abstract

Electrochemical CO_2 reduction (ECR) promises replacement of fossil fuels as the source of feedstock chemicals and seasonal storage of renewable energy. While much progress has been made in catalyst development and electrochemical reactor design, few studies have addressed the effect of catalyst integration on device performance. Using a microfluidic gas diffusion electrolyzer, we systematically studied the effect of thickness and morphology of electron-beam (EB) and magnetron-sputtered (MS) Cu catalysts coatings on ECR performance. We observed that EB Cu outperforms MS Cu in current density, selectivity, and energy efficiency, with 400 nm thick catalyst coatings performing best. The superior performance of EB Cu catalysts is assigned to their facetted surface morphology and sharper Cu/gas diffusion layer interface which increases their hydrophobicity. Tests in a large scale zero-gap electrolyzer yielded similar product selectivity distributions with an ethylene Faradaic efficiency of 39% at 200 mA/cm^2, demonstrating the scalability for industrial ECR applications.

Introduction

Coupling electrochemical conversion of the greenhouse gas CO_2 with renewable electricity sources such as solar and wind promises carbon-neutral production of high-demand chemicals and transportation fuels for a high-productivity and sustainable future.[1-2] This technology becomes increasingly competitive as prices of electricity from renewable energy resources continue to decrease.[2-3] Potential products of the electrochemical CO_2 reduction reaction (eCO_2RR), such as ethylene, ethanol, and acetic acid, can be used to feed industrial chemical process lines and power vehicles.[1-2, 4] At the same time, eCO_2RR provides an economical pathway for large-scale, seasonal storage of intermittent renewable electric energy. Much work has been devoted to developing more efficient electrochemical membrane reactor designs and catalyst materials.[5-13] Both micro-fluidic and zero-gap gas diffusion electrolyzer designs have shown great potential for realization of high current density eCO_2RR by directly delivering the reactant CO_2 to the catalyst in the gas phase.[9, 14-17] The four orders of magnitude higher diffusivity of CO_2 gas (16 mm^2/s) compared to CO_2 in an aqueous solution (0.0016 mm^2/s) effectively mitigates mass transport limitations.[18] These reactor designs require good control of the interface between the catalyst, electrolyte, and membrane because the overall performance of the CO_2 electrolyzer is largely influenced by the nature of these interfaces. For instance, a low hydrophobicity of the electrode-electrolyte interface likely causes flooding issues thus preventing the reactant (i.e., CO_2 gas) from reaching the catalyst for the reaction.[9] Many of the electrodes used in electrolyzer studies are fabricated through the deposition of the catalyst onto a porous carbon paper commonly known as the gas diffusion layer (GDL). The GDL consists of a fibrous backing for efficient mass transport and a microporous carbon layer as catalyst support. Both layers contain polytetrafluoroethylene (PTFE) to increase hydrophobicity for reducing the risk of flooding. Replacing the carbon backing by a PTFE layer and tuning the PTFE content in the microporous layer have both been used to further improve the GDL's flooding resilience.[9]

So far, copper and its alloys remain the only catalysts that have been demonstrated to efficiently convert CO_2 into multi-carbon (C_{2+}) products, such as ethylene, ethanol, acetate, and propanol. Previous studies focused primarily on understanding the effect of the copper catalyst morphology and composition on the eCO_2RR performance.[5, 7, 10, 19-26] Compared to catalyst and electrolyzer design, far fewer studies have addressed catalyst integration despite its critical importance on overall device performance and electrolyzer size upscaling. Hand, screen, spray, and inkjet painting are frequently used methods for applying the catalyst coating on the GDL or the electrolyzer membrane.[27-29] While all these methods are scalable towards larger electrodes and generally can provide good thickness and uniformity control (with exception of hand brush painting), they require development of suitable and stable particle-based ink systems. Furthermore, the particle character of the resulting catalyst coatings can cause poor electrical connectivity and mechanical properties. For example, Kenis *et al.*[28] reported on the effect of ink slurry deposition on eCO_2RR performance, comparing hand painting, air brushing, and screen printing methods. But despite critical importance for industrial applications, few studies have systematically addressed the effect of deposition method and Cu catalyst coating thickness on eCO_2RR performance, especially for flow cell electrolyzer configurations.

In this work, we used physical vapor deposition methods to systematically explore the effect of Cu catalyst coating thickness and morphology on eCO_2RR activity and selectivity in a three-compartment microfluidic electrolyzer. Compared to ink-based methods, physical vapor deposition methods provide superior control over thickness, especially at low catalyst loadings, and adhesion while their monolithic character reduces the contact resistance and provides mechanical stability.[30] Here, we used electron beam (EB) deposition and magnetron sputtering (MS) to deposit Cu coatings of various thicknesses on commercial GDLs. Both methods have the potential for large scale production, allow for direct coating of the electrocatalyst on the GDL, provide excellent thickness control and coating uniformity combined with high specific surface area. More importantly, they are also scalable to very large electrode areas ($\sim 10^4$ cm^2)[31-32] and enable precise control over morphology and porosity.[33-34] Physical vapor deposition methods also provide a path forward to efficient integration and compositional tuning of Cu alloy catalysts including non-thermodynamic equilibrium alloy compositions that are difficult to synthesize and integrate otherwise.[35-36] Beyond providing excellent control over coating uniformity, thickness, and composition, physical vapor deposition methods produce less waste and are less labor-intensive than traditional electrodeposition methods, thus making them cost competitive, despite higher capital costs.[37] Using a microfluidic gas diffusion electrolyzer, we observed that EB-Cu coatings generally provide better performance than the MS-Cu catalyst coatings in terms of current density, selectivity, and energy efficiency, with an optimum thickness of 400 nm where the energy efficiency (i.e., sum over the Faradaic efficiency times theoretical cell potential divided by the applied potential for all eCO_2RR products, for details see below) reaches 51% (56.5% for eCO_2RR and HER combined). Scanning and transmission electron microscopy (SEM/TEM), Rutherford backscatter analysis (RBA), electrochemical surface area (ECSA) and contact angle measurements suggest that the generally better eCO_2RR performance of EB-Cu coatings correlates with the GDL/Cu catalyst morphology making the EB-Cu catalyst layer more hydrophobic. Experiments performed in a large electrode area zero-gap electrolyzer yielded 39% ethylene Faradaic efficiency for both the EB- and MS-Cu coatings, demonstrating performance scalability of the two catalyst deposition methods for eCO_2RR.

Materials and Methods

Catalyst coatings

100-800 nm thick Cu films (Cu loading: 0.09 - 0.72 mg/cm^2) were deposited onto 25-600 cm^2 GDL substrates (Sigracet 39 BC) by both direct current (DC) magnetron sputtering (MS) and electron beam (EB) evaporation. Before coating, the GDL substrates were loaded into the respective deposition systems and pumped overnight to a base pressure in the 10^{-7} Torr range. The MS-Cu coatings were prepared at room temperature in a custom-built deposition chamber equipped with a three-inch magnetron sputtering gun and using a pure copper target (Process

Materials Inc, 99.99%), research grade Argon (99.9999%, chamber pressure 2 mTorr, flow rate 20 sccm) as a sputter gas, and a DC plasma power between 25 W and 100 W. Before every coating, the Cu target was pre-sputtered on the back of a shutter for approximately five minutes to remove any oxide layer on the surface of the copper target. Calibration runs were performed to determine the deposition rate by measuring the film thickness on silicon reference wafers with an Alpha-Step D-600 Stylus profilometer (KLA Tencor). The EB coatings were prepared in a custom-built EB system with a 10-kV power supply (Temescal) and a pure 15cc copper starter source (Process Materials Inc, 99.99%). The power supply was operated at 6.5 kV between 25-35% power to achieve deposition rates between 1.8 and 2.5 Å/s. A quartz crystal monitor (calibrated against a silicon witness sample) was utilized for in-situ monitoring the coating thickness.

Materials characterization

Transmission electron microscopy (TEM) measurements were performed on a FEI Titan 80 – 300 (scanning) transmission electron microscope operated at 300 kV. TEM samples were prepared by scratching the GDL Cu coatings with a clean scalpel blade and subsequently rubbing them against a lacey carbon TEM grid. The material composition was confirmed via energy dispersive x-ray spectroscopy (EDS) using the SuperX G2 detector in the Titan. Scanning electron microscope (SEM) measurements were performed on an Apreo SEM (Thermo Scientific) operated at an accelerating voltage of 5 keV with a working distance of 8 mm. For characterization of the Cu catalyst after long-term stability testing, SEM measurements were conducted on an Auriga 60 CrossBeam system.

The thickness and depth distribution of Cu in the prepared GDEs was studied by Rutherford backscattering spectrometry (RBS)[38] using 2 MeV $4He^+$ ions incident between 0 and 10° to the sample surface (to minimize ion channeling in the textured films) and backscattered into a detector at 164° from the incident beam direction. To extract the Cu depth distribution in the GDEs, we used the RUMP code.[39] In the RUMP simulations, the film was sliced into multiple layers to obtain the concentration depth profile. Conversion into depth scale assumes that the carbon in the MPC layer has a full density of 2.25 g/cc and a porosity of 75%.

For X-ray photoelectron spectroscopy (XPS) analysis of the catalyst after stability testing, the post reaction Cu electrode was first taken out of the electrolyzer, followed by washing with deionized water and drying. The electrode was stored in a vial filled with Ar before being analyzed by XPS (K-alpha Alpha X-ray photoelectron spectrometer system, Thermo Fisher Scientific). During the whole procedure, the electrode was exposed to air for less than 30 minutes. High-resolution XPS measurements were obtained by scanning the Cu 2p region 10 times with the flood gun turned on, using a pass energy of 20 eV and a step size of 0.1 eV. All peaks were fitted using Thermo Advantage software with adventitious carbon referenced to the C1s peak at 284.8 eV.

Electrochemical surface area analysis (ECSA)

Cu foil (Alfa Aesar), EB and MS-Cu samples were cut into 0.5 cm × 2 cm pieces and attached to a nickel wire using colloidal silver paint. The ECSA measurements were performed in a H-cell using a three-electrode configuration with a graphite rod counter electrode and a Ag/AgCl reference electrode, and a 0.1 M $HClO_4$ electrolyte under Ar atmosphere. For each sample, we recorded a series of cyclic voltammograms (CVs) in the pure double layer capacitance (C_{dl}) potential range (-0.12 V to 0.07 V *vs*. RHE) at scan rates ranging from 20 mV/s to 100 mV/s. The C_{dl} values were then calculated from current densities *vs*. scan rate plots. The ECSA of each sample and the corresponding roughness factor were obtained by normalizing the measured C_{dl} values to the C_{dl} value obtained from a Cu foil.

Electrochemical CO_2 reduction testing

The GDEs were cut into 0.5 cm × 2 cm pieces to fit into microfluidic flow cell set-up described previously[15] (Fig. S1). Most of the electrochemical measurements were performed in a three-electrode configuration with a Hg/HgO reference electrode and an Ir-coated carbon paper with a titanium foil current collector as the counter electrode. CO_2 was regulated with a mass flow controller (MKS Instruments) at a rate of 15 sccm, and 1 M KOH was used as both catholyte and anolyte and fed at a rate of 1.5 ml/min using peristatic pumps. The gas flow rates at the electrolyzer outlet were monitored using a gas flow meter (Agilent); no significant loss of CO_2 due to reaction with the 1 M KOH catholyte was found, and thus no corrections of the FE data were needed. After setting up the testing station, the current interrupt procedure was applied to measure the resistance before testing. No trend for resistance *vs* thickness was observed. The tests were conducted at constant current mode using a potentiostat (Autolab), and the potentials were recorded at the times of sample collection and corrected with the pH of the electrolyte and the measured resistance to the Reversible Hydrogen Electrode (RHE) scale (V [*vs* RHE] = V [Hg/HgO] + 0.098 + 0.059 × 14 + $I \times R$, where I is the current density and R is the measured resistance). To quantify the products, the gas outlet was fed to the GC (SRI Instruments), and liquid electrolyte samples were collected at different times, diluted with DI water, and analyzed through NMR (AVIII 600).

To demonstrate scalability and study the effect of electrolyzer environment on catalyst performance, supplementary eCO_2RR experiments were conducted in a zero-gap, membrane-based 25 cm^2 electrolyzer at Twelve Inc. These electrochemical tests used an Aemion™ HNN8-

50 (Ionomr Innovations Inc.) alkaline exchange membrane (AEM) to separate the Cu cathode GDE from a IrO_x-coated porous Ti anode (Fig. S1b). The membrane electrode assembly (MEA) was compressed between two flow fields against the respective cell current collectors. CO_2 gas was directly fed into the cathode side of the electrolyzer at a flow rate of 250 sccm, while KOH electrolyte (0.5 M) was circulated via a peristaltic pump on the anode side at a rate of 60 mL/min. Electrolysis was run in the constant current mode with 35-minute holds at 100, 200, and 250 mA/cm^2. Gas products were analyzed by GC equipped with both flame ionization detector (FID) and thermal conductivity detector (TCD). The FEs reported using the zero-gap electrolyzer are corrected for CO_2 crossover.

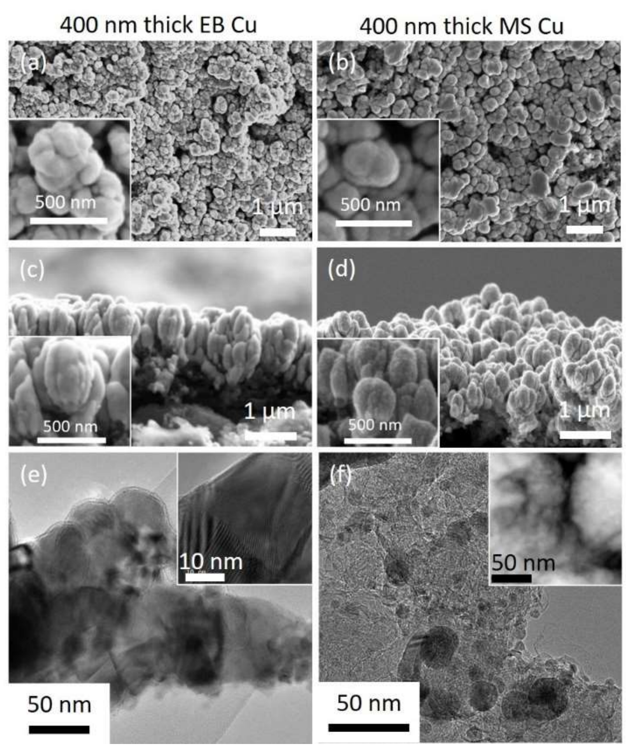

Figure 1: Characterization of Cu catalyst coatings: Top view SEM micrographs of (a) 400 nm thick EB and (b) MS Cu coatings on GDLs, as wells as the corresponding cross-sectional SEM images (c,d); TEM micrographs of 100-nm-thick EB (e) and MS (f) Cu coatings.

Results and Discussion

Characterization of Cu catalysts on GDL

The microstructure of EB- and MS-Cu coatings on the microporous carbon (MPC) top layer of the GDLs was characterized by SEM and TEM (Figure 1). While the Cu coatings fabricated by both methods become increasingly dense with increasing coating thickness, even the thickest, 800 nm thick Cu films on the porous GDL substrate remain porous in nature (Figure S2). The open porous microstructure of the Cu coatings is a critical feature for eCO_2RR as it enables fast transport of the gaseous reactant CO_2 through the GDL to the catalyst layer as required for realization of high eCO_2RR current densities (> 100 mA/cm^2). A comparison of SEM images collected from the top surface of nominally 400 nm thick EB (Figure 1a) and MS (Figure 1b) Cu coatings reveals that both films consist of 100-400 nm diameter Cu particles. However, the EB-Cu nanoparticles seem to have more well-defined facets, while the MS-Cu particles have a very rough and serrated appearance. The corresponding cross-sectional SEM images (Figure 1c and d) confirm the open porous character of the Cu coatings and suggest the presence of a relatively sharp transition between the MPC layer (dark) of the GDL and the Cu catalyst layer (bright). TEM further confirms the more ordered, facetted nature of the EB-Cu coatings suggested by the SEM images. The EB-Cu particles consist of well-defined grains of about 10-50 nm and have a facetted surface (Figure1e); the MS-Cu particles seem to be composed of smaller, irregular shaped nanocrystals (Figure 1f), and the surface is very rough even at the highest resolution.

For a more quantitative characterization of the depth distribution of the Cu coatings on and within the MPC layer of the GDLs, we turned to Rutherford backscattering spectrometry. Representative RBS spectra of nominally 400 nm thick EB- and MS-Cu coatings on the GDL substrate are shown in Figure 2a and 2b, respectively. Composition and depth distribution (Figure 2c) of the Cu coatings were obtained by fitting of the RBS spectra shown in Figure 2a,b using RUMP code[39] simulations. The surface peaks of ^{64}Cu, ^{19}F (from the PTFE content of the MPC layer of the GDL), and ^{12}C are marked by arrows. The actual thickness of the Cu coating was estimated by fitting the RBS signal between the Cu surface peak and the 50% signal on the low energy side of the spectra (dashed line in Figure 2a,b). The coating thickness thus derived is in good agreement with the nominal thicknesses predicted from the measured Cu depositions rates on flat substrates; for example, for nominally 400 nm thick EB- and MS-Cu films the RBS Cu coating thickness is 394 and 358 nm, respectively. The signal between the Cu surface peak and the Cu/MPC-PTFE interface (marked by ↓Cu/PTFE) corresponds to pure Cu deposited on top of the MPC layer of the GDL. Here, the Cu/MPC-PTFE interface is defined by the first data point where the measured signal drops 10% below the simulated signal for pure copper (dashed line in Figure 2a and b). The spectral intensity in the region between the Cu/MPC-PTFE interface and the ^{19}F surface peak can be attributed to Cu deposited within the MPC layer of the GDL, and the solid line is the result of a RUMP code simulation based on fitted Cu-to-C atomic ratio depth profiles shown in Figure 2c. The depth profile analysis reveals that the Cu-to-C ratio in the MPC layer of the EB coated GDL is lower than that of the MS GDL. The higher gas pressure used for magnetron sputtering seems to facilitate the deposition of Cu within the MPC layer of the GDL. Similar trends were observed for both thinner and thicker Cu coatings, although the effect seems to become less pronounced for thicker coatings. Both the different surface morphology revealed by SEM and TEM (Figure 1) and the different Cu-MPC interface (Figure 2a-c) can be expected to affect the nature of the solid/liquid/gas triple phase boundary that is critical for the performance of a GDE.

Contact angle measurements on GDEs with nominally 400 nm thick EB (Figure 2d) and MS (Figure 2e) Cu films indeed confirm that the different surface and MPC/Cu interface morphology of EB and MS films affects the wetting behavior of the GDEs. The contact angle measurements were performed on 400 nm thick catalyst coatings because they provided the overall best eCO_2RR performance (see below) as both thinner and thicker coatings resulted in lower electrochemically accessible surface areas (Fig. 2f). With a contact angle of 124° compared to 65° the EB-Cu/GDE sample of the GDE is significantly more hydrophobic than the corresponding MS-Cu/GDE sample. For comparison, the contact angle of the fibrous backing side of the GDE is also 124° (Figure S3). We note that the as-deposited Cu catalyst coatings used for the contact angle experiments have a few nm-thick native oxide layer[40] that can be expected to make the Cu coatings less hydrophobic than under eCO_2RR operation. In general, the wetting behavior of the hierarchically structured catalyst coatings is poorly understood as it depends on many parameters including surface chemistry, meso- and nano-scale surface roughness as well as applied electrochemical potential.[18, 41-43]

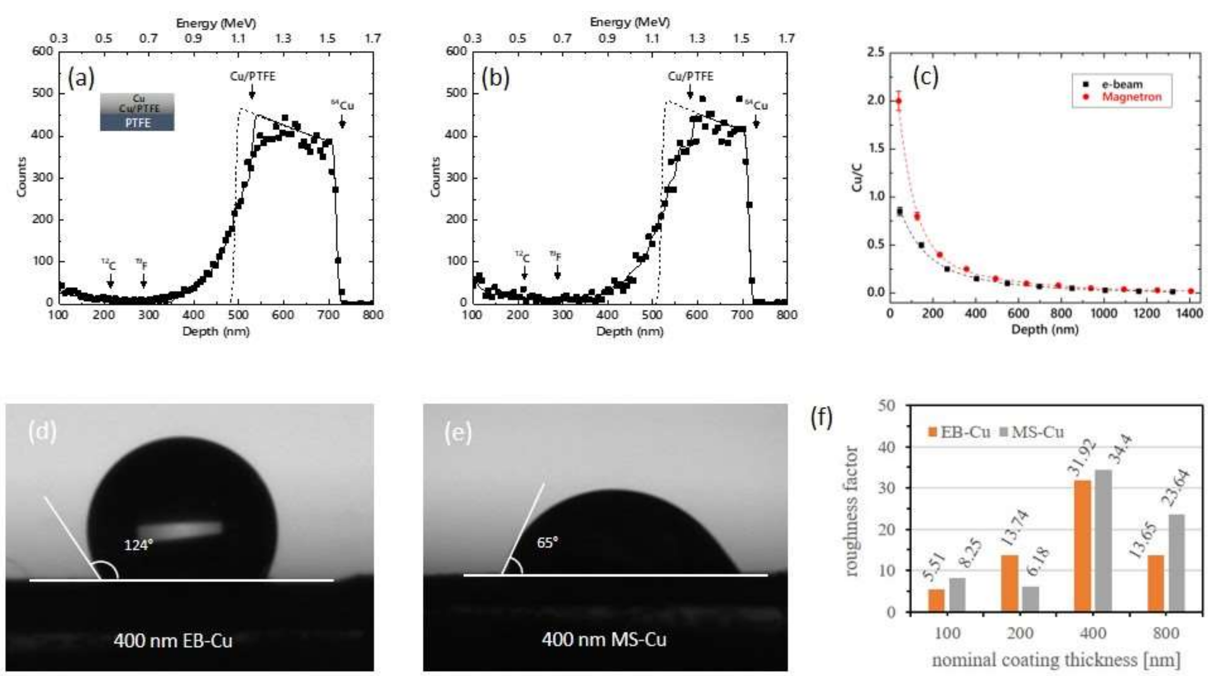

Figure 2: RBS spectra from GDEs with nominally 400 nm thick EB-Cu (a) and MS-Cu (b) coatings. The surface peaks of ^{64}Cu, ^{19}F (from the PTFE content of the MPC layer), and ^{12}C are

denoted by arrows. Dashed lines are RUMP simulations for 394 (a) and 358 nm (b) fully dense Cu coatings on MPC, and solid lines are the result of RUMP code simulations reflecting the Cu-to-C depth distribution in the MPC layer shown in (c); contact angle measurements on GDEs with nominally 400 nm thick EB (d) and MS-Cu (e) coatings; (f) EB/MS-Cu roughness factor vs. thickness values derived from ECSA measurements shown in Figure S4 and S5.

The ECSA of the GDEs was measured by electrochemical double layer (DL) capacitance measurements in an Ar saturated 1 M $HClO_4$ electrolyte (Figure S4 and Figure S5). CVs of 400 nm EB Cu-GDEs are shown in Figure S4a. The corresponding current density *vs*. scan rate plots (Figure S4b) show the expected linear behavior for pure capacitive DL charging. The roughness factor vs. thickness plot (Figure 2f), obtained by using the measured area specific capacitance of a Cu foil of 25 $\mu F/cm^2$ as a reference (Figure S4c), reveals that the ECSA increases approximately linear between 100 and 400 nm EB Cu coating thickness with a maximum roughness factor of ~32, but deceases again for thicker Cu films indicating that for the thickest coatings some of the porosity becomes inaccessible. Similar trends with on average slightly higher roughness factors for nominally identical thicknesses have been observed for the MS-Cu coated GDEs (Figure 2f and Figure S5).

Evaluation of vapor deposited Cu catalysts for eCO_2RR

To explore if and how the different Cu catalyst surface morphology, Cu/MPC interface structure, and wetting behavior affects the eCO_2RR performance, nominally 400 nm thick EB and MS Cu catalysts films were tested using a three-compartment microfluidic flow cell for CO_2 electrolysis (Figure 3). Both samples show the product spectrum expected for eCO_2RR over polycrystalline copper.[10, 15, 44] The Faradaic efficiencies (FEs) for ethylene, ethanol, and acetate go up with increasing potential/current density while that of CO decreases. However, there are distinct differences in the performance in terms of selectivity, current density, and stability: Compared to the MS Cu sample, the 400 nm EB Cu sample 1) reaches the highest current density (400 mA/cm^2) at lower overpotentials (-0.65V vs. RHE for EB-Cu compared to -0.83 V vs. RHE for MS-Cu), and 2) better suppresses the competing hydrogen evolution reaction (HER), especially for high current densities; for the highest current density of 400 mA/cm^2, H_2 FE for MS-Cu (28%) is 4 times higher than for EB-Cu (7%). For 400 nm EB-Cu, C_{2+} FE reaches 70% at the highest current density of 400 mA/cm^2. As the total current density increases to 400 mA/cm^2 for the MS-Cu sample, the voltage becomes unstable, and the cathode suffers from flooding issues despite setting the CO_2 backpressure to 15 psi as an attempt to stabilize the gas/liquid interface. We attribute these differences to the more hydrophilic character of MS-Cu coatings as revealed by the contact angle measurements (Figure 2d,e) which may be further amplified by electrowetting[45] given the more negative potentials that need to be applied for driving higher current densities on MS-Cu GDEs. In the microfluidic electrolyzer setup used for these experiments (Figure S1a) the catalyst layer is in direct contact with a thin layer of liquid electrolyte, and the hydrophobicity of the GDE is thus crucial to prevent flooding which blocks the CO_2 supply at the Cu catalyst.[15] The rougher nanoscale surface morphology and the thicker Cu/MPC interface of the MS-Cu coating seem to lower the GDL hydrophobicity resulting in more liquid penetrating the catalyst layer thus shifting the selectivity towards HER. While the morphology of the coatings may in principle evolve during eCO_2RR operation thus changing the wetting behavior, post-operation characterization of the Cu catalyst coatings (see below) did not provide evidence for pronounced morphology changes. Finally, we note that among the many deposition parameters that can be changed, the deposition angle is probably one of the most important parameters as it allows one to control the film porosity.[33] Indeed, preliminary oblique angle coating experiments indicate further improvement of the eCO_2RR performance.

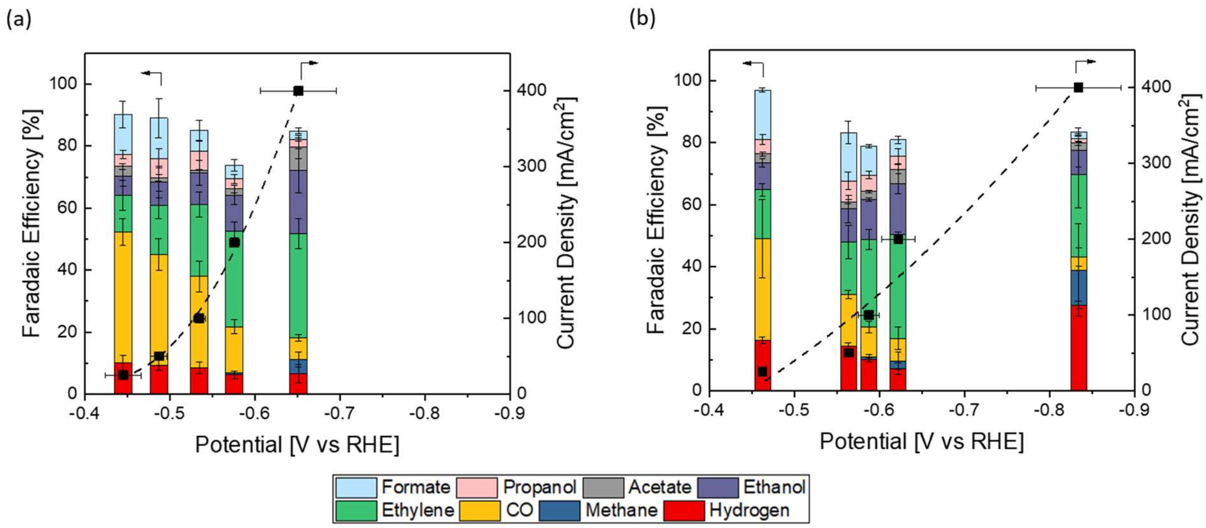

Figure 3: Faradaic efficiencies and current densities vs. potential for eCO_2RR with 400 nm (a) EB-Cu and (b) MS-Cu catalysts. These tests were conducted in a three-compartment flow cell, with 15 sccm CO_2 and 1 M KOH electrolyte at room temperature.

Effect of Cu catalysts thickness on eCO_2RR performance

The effect of thickness of the EB-Cu catalysts coating on current density and eCO_2RR performance is summarized in Figure 4. Because the results discussed above revealed that the EB-Cu coatings outperform MS-Cu coatings in terms of selectivity, current density, and stability, we focused on EB-Cu coatings. The corresponding plots of Faradaic efficiencies and current densities *vs.* potential are shown in Figure S6. In general, the eCO_2RR performance of the EB-Cu catalyst improves with increasing the catalyst loading. The overpotential required for any given current density decreases as the EB coating thickness increases, with the best performance observed for 400 nm thick EB Cu coatings that required the lowest overpotential (-0.65V vs RHE) for reaching

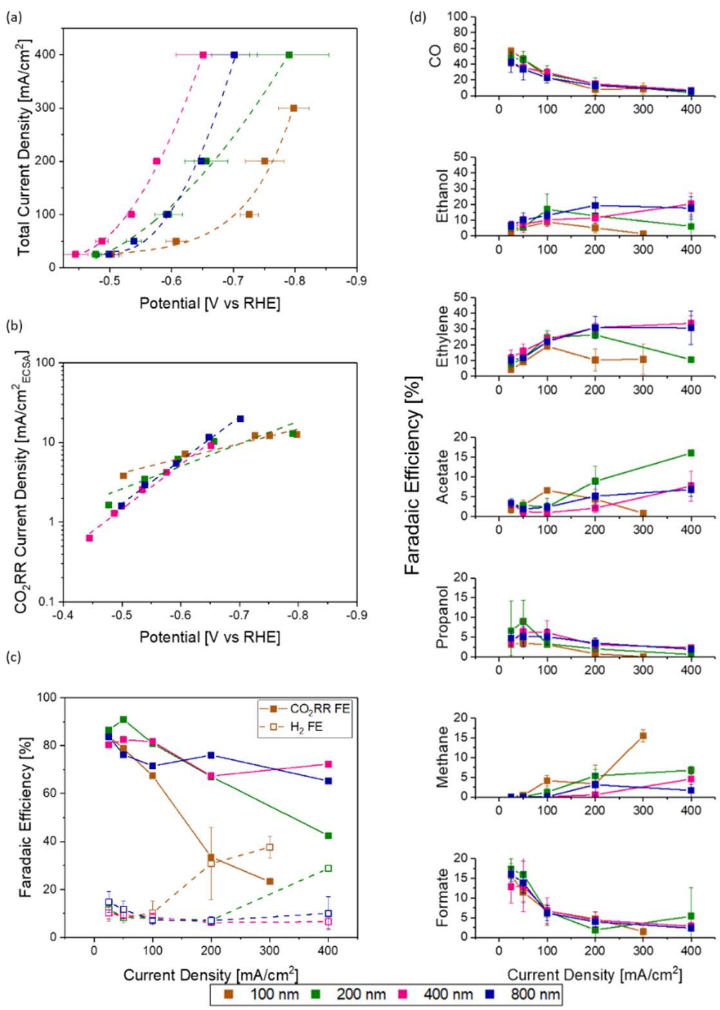

Figure 4: Comparison of the eCO_2RR performance of EB-Cu samples of different thicknesses (100, 200, 400, and 800 nm) measured in a 3-compartment electrochemical flow cell (Figure S1a), with 15 sccm CO_2 and 1 M KOH electrolyte. (a) Total current densities vs. potential for all the thicknesses; (b) ECSA-normalized eCO_2RR current densities for each catalyst; (c) HER and eCO_2RR Faradaic efficiencies for all the different thicknesses at different current densities; and (d) FE of eCO_2RR products (CO, methane, formate, ethylene, ethanol, acetate, propanol) vs. current density.

a current density of 400 mA/cm^2 (Figure 4a). For thicker Cu catalysts coatings (800 nm) the overpotential increases again. Normalizing the eCO_2RR current density by the ECSA measured for the different coating thicknesses (Figure 2f) reveals that, regardless of the Cu loading, the coating thickness has little effect on the intrinsic activity of Cu, especially at the lower potentials (Figure 4b). It also indicates that the entire ECSA contributes to eCO_2RR. A closer look at the area normalized current density reveals that the higher current density data of the thinner 100/200 nm thick Cu coatings start to deviate from the linear behavior. To summarize, while it is well known that the ECR performance depends on the morphology and particle size of Cu catalyst coatings,[9, 15] we believe that for the catalyst coatings studied in the present work, the main effect of increasing the coating thickness on eCO_2RR performance is increasing the roughness factor as the coating thickness seems to have little effect on the intrinsic activity of Cu.

The coating thickness also affects the selectivity towards HER and eCO_2RR (Figure 4c,d): For high current densities, the increase in HER can be suppressed by using thicker EB-Cu coatings (increasing the catalyst surface area) (Figure 4c). For example, increasing the EB-Cu coating thickness from 100 (200) nm to 400 nm reduces H_2 FE by about a factor of 6 (5) times, from 37.7% at 300 mA/cm^2 for 100 nm Cu and 28.8% at 400 mA/cm^2 for 200 nm Cu to 6.7% at 400 mA/cm^2 for the 400 nm EB-Cu coating. The suppression of HER with increasing Cu coating thickness is accompanied by an increase in eCO_2RR FE, from 23.2% (42.5%) at 300 (400) mA/cm^2 for 100 (200) nm EB-Cu to 72% at 400 mA/cm^2 for 400 nm EB-Cu (Figure 4c). The suppression in HER with increasing roughness factor has also been observed for electrochemical CO reduction although at 100 times lower current densities.[46] The increase in eCO_2RR selectivity with increasing Cu catalyst loading can be attributed to the higher Cu catalytic surface area available for eCO_2RR (Figure 2f and Figure S3). Consequently, the smaller Cu catalytic surface area of 800 nm EB-Cu coatings compared to 400 nm EB-Cu coatings (Figure 2f and Figure S4) explains the increase observed for both the required overpotential (Figure 4a) and H_2 FE (Figure 4c). The reduced ECSA for the 800 nm sample is also evident in the SEM images (Figure S2), in which the 800 nm sample shows more aggregation and less porosity than the 400 nm sample.

The eCO_2RR product distributions at different current densities for all the Cu catalysts are shown in Figure 4d. CO and formate FEs decrease with increasing current density while the C_2 FEs (i.e., ethylene, ethanol and acetate FEs) increase with increasing current density, but only for the thicker Cu coatings (400 and 800 nm). The methane FE shows a maximum (15%@ 300 mA/cm^2) for the highest current density – lowest coating thickness combination. The propanol FE is always low and shows no obvious dependence on current density or coating thickness. In summary, the most important effect of film thickness is that the selectivity for C_2 products at the highest current densities increases with increasing Cu loading. The effect of surface area / roughness factor on selectivity has recently also been reported for electrochemical CO reduction where the selectivity towards oxygenates increased with increasing roughness factor, although measured at much lower current densities (< 1 mA/cm^2).[46]

Energy efficiency analysis and long-term stability

An energy efficiency analysis confirms that the 400 nm EB-Cu catalyst coating provides the best combination of overpotential, eCO_2RR FE, and current density, with a total (eCO_2RR and HER combined) energy efficiency of 56.5% at 400 mA/cm^2 (Figure 5). The energy efficiency was calculated using Faradaic efficiencies for each detected product including hydrogen (Figure 4) using the following formula:

$$\varepsilon_{energetic} = \sum_{k} \frac{\varepsilon_{Faradaic,k} E^{\circ}{}_{k}}{E_{applied}}$$

where $\varepsilon_{Faradaic,k}$ is the Faradaic efficiency for product k, $E^{o}{}_{k}$ are the thermoneutral theoretical potentials for these products[47] shown in the table S1, and $E_{applied}$ is the estimated full cell potential assuming no overpotential for oxygen evolution on the anode. For all catalyst coating thicknesses, the total energy efficiency decreases with increasing current density, from ~70% for 25 mA/cm^2 to ~50% for 400 mA/cm^2 (Figure 5a). For the highest current density (400 mA/cm^2), the total (eCO_2RR + HER) energy efficiency (56.5%) and especially the eCO_2RR energy efficiency (51%) peak at 400 nm EB Cu (Figure 5b). Note, that the maximum current density for the 100 nm EB Cu coating reached only 300 mA/cm^2.

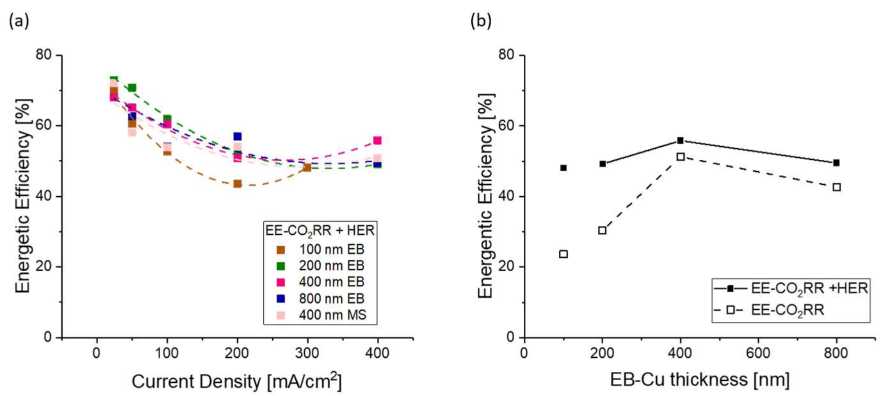

Figure 5: (a) Energy efficiency (eCO_2RR + HER) vs. current density for 100-800 nm EB Cu and 400 nm MS Cu catalyst coatings, and (b) energy efficiency vs. film thickness at the highest current density measured (300 mA/cm^2 for 100 nm EB-Cu, 400 mA/cm^2 for all other thicknesses). All tests were performed in the three-compartment flow cell (Figure S1a) using 15 sccm CO_2 and 1 M KOH electrolyte.

Extended eCO_2RR tests with a 400 nm EB-Cu catalysts coating showed a stable performance (Figure 6). This test ran for almost 6 hours, before H_2 FE started to increase. The potential gradually increased by ~15% over time where the increase slightly accelerated at the onset of the increase of H_2 FE after 4 hours. Post-reaction characterization through XPS and SEM imaging

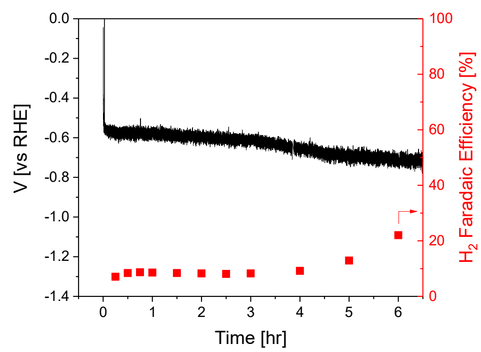

Figure 6: Electrode potential vs. RHE and FE(HER) during a long-term stability test of 400 nm EB-Cu in the microfluidic electrochemical flow cell at a constant current density of 100 mA/cm^2 with 15 sccm CO_2 and 1 M KOH electrolyte.

(Figure S7) revealed that the catalyst morphology and composition did not change during the test suggesting that the catalyst is not responsible for the degrading performance after 5 hours. XPS (Figure S7a) further showed that preexisting Cu^{2+} oxides have been reduced during the eCO_2RR. During the testing, water droplets and salt buildup were observed on the back of the GDL (Figure S7b) suggesting that catholyte has permeated through the GDL (despite controlling the gas-liquid interface through a back pressure controller set at a constant 14.75 psi) resulting in partial blockage of the GDL for gas delivery. We note that the long-term stability of current state-of-the-art CO_2-to-fuel electrolyzers is a device level problem and limited, for example, by the stability of the membrane and management of water as well as low-vapor-pressure eCO_2RR products. For example, a recent study demonstrated that even in a microfluidic GDE electrolyzer with a catholyte flow field, enrichment of lower volatility products such as ethanol at high current densities can change the wetting behavior of the GDE leading to electrolyte penetration, causing stability issues and mass transport limitations.[48] Similarly, the stability of zero-gap electrolyzers has been reported to be limited by salt precipitation as well as condensation of water and low-vapor-pressure eCO_2RR products in the flow field channels.[18] For long-term stability testing, it will thus be necessary to not only optimize the catalyst integration but also the GDL catalyst support to withstand flooding and prevent salt buildup during prolonged operations.

To demonstrate scalability and assess the effect of local environment on the performance of EB and MS Cu catalyst films, we also performed tests in a zero-gap, membrane-based electrolyzer that has a larger area (25 cm^2) compared to the microfluidic flow reactor and is optimized for industrial applications. In the zero-gap gas diffusion electrolyzer the Cu GDE was in direct contact with an AEM instead of KOH catholyte used in the microfluidic electrolyzer. The main advantages of the zero-gap gas-diffusion electrolyzer configuration is that this design is more straightforward to scale up, minimizes resistive losses of the device by minimizing the diffusion distance between the cathode and anode and is more robust against cathode flooding. This configuration, however, makes integration of a reference electrode and detection of liquid products more difficult. Both 400 nm thick EB and MS Cu coatings reach ethylene FEs of at least 30%, with a maximum of 39% at 200 mA/cm^2 while the competing HER stayed below 20% (Figure 7). While the performances of ES and MS Cu GDEs in terms of FE ethylene are more similar than in the microfluidic configuration, the EB Cu GDE still suppresses the parasitic HER more effectively than the MS Cu GDE like it was observed for the microfluidic configuration although the effect is, as expected, less pronounced. Likewise, the missing FE is attributed to the low vapor pressure products (ethanol, propanol, acetate) that are difficult to detect in our current zero-gap gas-diffusion electrolyzer design. In summary, the results from the larger electrolyzer testing demonstrate that the two catalyst deposition methods are scalable for eCO_2RR, which leads to further commercial viability of this technology.

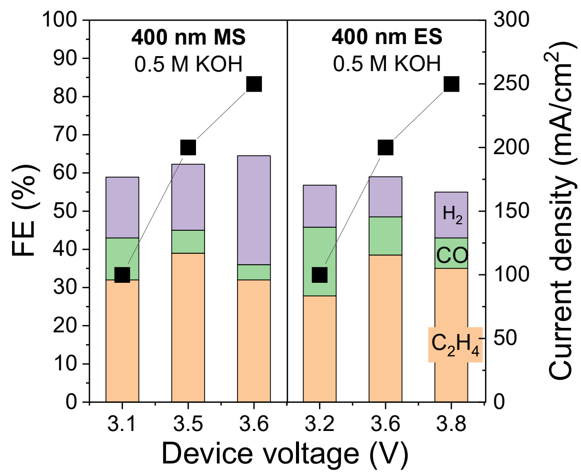

Figure 7: FE (%) for H_2, CO, and C_2H_4 plotted at 100, 200, and 250 mA/cm^2 applied current densities as a function of full cell voltage for 400 nm EB and MB Cu catalysts coatings tested in a zero-gap gas-diffusion electrolyzer

Conclusion

The effect of catalyst deposition methods and loading on eCO_2RR performance was assessed in a microfluidic gas diffusion electrolyzer. EB-Cu catalysts showed generally better performance than the corresponding MS-Cu catalysts coatings which is attributed to the more hydrophobic character of EB Cu GDLs. RBS and TEM analysis revealed that more MS Cu is deposited within the MPC layer of the GDL, and that the MS Cu coatings are rougher than the corresponding EB Cu coatings, both rendering MS Cu catalyst coatings less hydrophobic and more prone to flooding. The thicknesses of the EB Cu samples also strongly affects device performance: Low Cu loadings (100 and 200 nm EB-Cu) result in higher overpotentials as well as lower FE for eCO_2RR and C_2H_4. The poorer performance of lower Cu catalyst loadings is attributed to the lower surface area available on these coatings. Increasing the Cu loading too much also reduced the eCO_2RR performance as seen with the 800 nm EB-Cu, causing aggregation of the catalyst resulting in lower porosity and less catalytic surface area, which also led to worse performance. For the optimal thickness of 400 nm, EB Cu reached a eCO_2RR energetic efficiency of 51% (56.5% for eCO_2RR and HER combined) and a C_{2+} FE of 70% at 400 mA/cm^2.

Preliminary tests of the same catalysts in a large area zero-gap electrolyzer showed similar performances in terms of current density, eCO_2RR/HER selectivity, and FE for ethylene production, demonstrating promising scalability for industrial applications. In summary, our works demonstrates that, despite little attention in the field, integration of eCO_2RR catalysts is of equal importance to compositional tuning, and that the catalyst integration needs to be optimized for the specific electrolyzer environment. In other words, caution must be exercised when comparing the performance of different eCO_2RR catalysts if the integration for these catalysts has not been optimized for the particular electrolyzer environment. The MS/EB PVD catalyst deposition techniques used in this work are particularly well-suited to optimize both integration and composition of eCO_2RR catalysts for large, industrially relevant electrolyzer electrodes as they allow the deposition of very homogeneous coatings with very uniform catalyst loading while at the same time enabling morphological and compositional tuning including non-thermal equilibrium alloy compositions that otherwise are difficult to integrate.

Supporting Information

SEM images of EB-Cu with different thickness; Contact angle on the back side of the GDL; Electrochemical surface area of EB-Cu and MS-Cu; electrochemical CO_2 reduction performance of EB-Cu in 3-compartment flow cell; Characterization of 400 nm EB-Cu after long-term stability test; Thermoneutral theoretical potentials table.

AUTHOR INFORMATION

Corresponding Author

jiao@udel.edu, biener2@llnl.gov

Author Contributions

E. Jeng, Z. Qi, A. R. Kashi, K. P. Kuhl, S. Ma, F. Jiao, J. Biener: designed the experiments. E. Jeng, Z. Qi, A. R. Kashi, S. Hunegnaw, Z. Huo, J. S. Miller, L. B. Bayu-Aji, B. H. Ko, H. Shin performed materials characterization and carried out electrochemical tests. E. Jeng, F. Jiao, J. Biener wrote the initial paper. The manuscript was written through contributions of all authors. All authors have given approval to the final version of the manuscript. †These authors Emily Jeng and Zhen Qi contributed equally.

Notes

A. R. K., S. H., Z. H., S. M., and K. P. K. have financial interest in Twelve Inc., a company commercializing the carbon dioxide electrolysis technology.

Acknowledgements

IM release number: LLNL-JRNL-821645. Emily Jeng and Zhen Qi contributed equally to this work. *Funding*: This work was supported by the U.S. Department of Energy's Office of Energy Efficiency and Renewable Energy (EERE) under the Advanced Manufacturing Office Next Generation R&D Projects award number DE-EE-0008327. The views expressed herein do not necessarily represent the views of the U.S. Department of Energy or the United States Government. The work was performed under the auspices of the US Department of Energy by LLNL under contract No. DE-AC52-07NA27344 and a Strategic Partnership Program agreement with TOTAL American Services, Inc. (affiliate of TOTAL SE) under contract No. L-21350. We are grateful for the nanofabrication and imaging facilities in the Molecular Foundry at the Lawrence Berkeley National Laboratory. Work at the Molecular Foundry was supported by the Office of Science, Office of Basic Energy Sciences, of the U.S. Department of Energy under Contract No. DE-AC02-05CH11231.

References:

(1) Bushuyev, O. S.; De Luna, P.; Dinh, C. T.; Tao, L.; Saur, G.; van de Lagemaat, J.; Kelley, S. O.; Sargent, E. H. What Should We Make with CO_2 and How Can We Make It? *Joule* **2018,** *2* (5), 825-832, DOI: 10.1016/j.joule.2017.09.003.

(2) De Luna, P.; Hahn, C.; Higgins, D.; Jaffer, S. A.; Jaramillo, T. F.; Sargent, E. H. What Would It Take for Renewably Powered Electrosynthesis to Displace Petrochemical Processes? *Science* **2019,** *364* (6438), eaav3506, DOI: 10.1126/science.aav3506.

(3) Haegel, N. M.; Atwater, H.; Barnes, T.; Breyer, C.; Burrell, A.; Chiang, Y. M.; De Wolf, S.; Dimmler, B.; Feldman, D.; Glunz, S.; Goldschmidt, J. C.; Hochschild, D.; Inzunza, R.; Kaizuka, I.; Kroposki, B.; Kurtz, S.; Leu, S.; Margolis, R.; Matsubara, K.; Metz, A.; Metzger, W. K.; Morjaria, M.; Niki, S.; Nowak, S.; Peters, I. M.; Philipps, S.; Reindl, T.; Richter, A.; Rose, D.; Sakurai, K.; Schlatmann, R.; Shikano, M.; Sinke, W.; Sinton, R.; Stanbery, B. J.; Topic, M.; Tumas, W.; Ueda, Y.; de Lagemaat, J. V.; Verlinden, P.; Vetter, M.; Warren, E.; Werner, M.; Yamaguchi, M.; Bett, A. W. Terawatt-Scale Photovoltaics:

Transform Global Energy. *Science* **2019,** *364* (6443), 836-838, DOI: 10.1126/science.aaw1845.

(4) Jhong, H. R.; Ma, S. C.; Kenis, P. J. A. Electrochemical Conversion of CO_2 to Useful Chemicals: Current Status, Remaining Challenges, and Future Opportunities. *Curr. Opin. Chem. Eng.* **2013,** *2* (2), 191-199, DOI: 10.1016/j.coche.2013.03.005.

(5) Hori, Y.; Wakebe, H.; Tsukamoto, T.; Koga, O. Electrocatalytic Process of CO Selectivity in Electrochemical Reduction of CO_2 at Metal Electrodes in Aqueous Media. *Electrochim. Acta* **1994,** *39* (11-12), 1833-1839, DOI: 10.1016/0013-4686(94)85172-7.

(6) Kortlever, R.; Shen, J.; Schouten, K. J. P.; Calle-Vallejo, F.; Koper, M. T. M. Catalysts and Reaction Pathways for the Electrochemical Reduction of Carbon Dioxide. *J. Phys. Chem. Lett.* **2015,** *6* (20), 4073-4082, DOI: 10.1021/acs.jpclett.5b01559.

(7) Lu, Q.; Rosen, J.; Jiao, F. Nanostructured Metallic Electrocatalysts for Carbon Dioxide Reduction. *ChemCatChem* **2015,** *7* (1), 38-47, DOI: 10.1002/cctc.201402669.

(8) Lu, Q.; Jiao, F. Electrochemical CO_2 Reduction: Electrocatalyst, Reaction Mechanism, and Process Engineering. *Nano Energy* **2016,** *29*, 439-456, DOI: 10.1016/j.nanoen.2016.04.009.

(9) Dinh, C. T.; Burdyny, T.; Kibria, M. G.; Seifitokaldani, A.; Gabardo, C. M.; de Arquer, F. P. G.; Kiani, A.; Edwards, J. P.; De Luna, P.; Bushuyev, O. S.; Zou, C. Q.; Quintero-Bermudez, R.; Pang, Y. J.; Sinton, D.; Sargent, E. H. CO_2 Electroreduction to Ethylene via Hydroxide-Mediated Copper Catalysis at An Abrupt Interface. *Science* **2018,** *360* (6390), 783-787, DOI: 10.1126/science.aas9100.

(10) Nitopi, S.; Bertheussen, E.; Scott, S. B.; Liu, X. Y.; Engstfeld, A. K.; Horch, S.; Seger, B.; Stephens, I. E. L.; Chan, K.; Hahn, C.; Norskov, J. K.; Jaramillo, T. F.; Chorkendorff, I. Progress and Perspectives of Electrochemical CO_2 Reduction on Copper in Aqueous Electrolyte. *Chem. Rev.* **2019,** *119* (12), 7610-7672, DOI: 10.1021/acs.chemrev.8b00705.

(11) Xie, J. F.; Chen, J. J.; Huang, Y. X.; Zhang, X.; Wang, W. K.; Huang, G. X.; Yu, H. Q. Selective Electrochemical CO_2 Reduction on Cu-Pd Heterostructure. *Appl Catal B-Environ* **2020,** *270*, 118864, DOI: 10.1016/j.apcatb.2020.118864.

(12) Zhi, X.; Jiao, Y.; Zheng, Y.; Vasileff, A.; Qiao, S. Z. Selectivity Roadmap for Electrochemical CO_2 Reduction on Copper-Based Alloy Catalysts. *Nano Energy* **2020,** *71*, 104601, DOI: 10.1016/j.nanoen.2020.104601.

(13) Zhang, B. H.; Jiang, Y. Z.; Gao, M. X.; Ma, T. Y.; Sun, W. P.; Pan, H. G. Recent Progress on Hybrid Electrocatalysts for Efficient Electrochemical CO_2 Reduction. *Nano Energy* **2021,** *80*, DOI: 10.1016/j.nanoen.2020.105504.

(14) Whipple, D. T.; Finke, E. C.; Kenis, P. J. A. Microfluidic Reactor for the Electrochemical Reduction of Carbon Dioxide: The Effect of pH. *Electrochem. Solid-State Lett.* **2010,** *13* (9), D109-D111, DOI: 10.1149/1.3456590.

(15) Lv, J. J.; Jouny, M.; Luc, W.; Zhu, W. L.; Zhu, J. J.; Jiao, F. A Highly Porous Copper Electrocatalyst for Carbon Dioxide Reduction. *Adv. Mater.* **2018,** *30* (49), 1803111, DOI: 10.1002/adma.201803111.

(16) Weekes, D. M.; Salvatore, D. A.; Reyes, A.; Huang, A. X.; Berlinguette, C. P. Electrolytic CO_2 Reduction in a Flow Cell. *Accounts Chem Res* **2018,** *51* (4), 910-918, DOI: 10.1021/acs.accounts.8b00010.

(17) Burdyny, T.; Smith, W. A. CO_2 Reduction on Gas-Diffusion Electrodes and Why Catalytic Performance Must Be Assessed at Commercially-Relevant Conditions. *Energ. Environ. Sci.* **2019,** *12* (5), 1442-1453, DOI: 10.1039/c8ee03134g.

(18) Weng, L.-C.; Bell, A. T.; Weber, A. Z. Towards Membrane-Electrode Assembly Systems for CO_2 Reduction: A Modeling Study. *Energ. Environ. Sci.* **2019,** *12* (6), 1950-1968, DOI: 10.1039/C9EE00909D.

(19) Hori, Y.; Takahashi, I.; Koga, O.; Hoshi, N. Electrochemical Reduction of Carbon Dioxide at Various Series of Copper Single Crystal Electrodes. *J. Mol. Catal. A Chem.* **2003,** *199* (1-2), 39-47, DOI: 10.1016/s1381-1169(03)00016-5.

(20) Kuhl, K. P.; Cave, E. R.; Abram, D. N.; Jaramillo, T. F. New Insights into the Electrochemical Reduction of Carbon Dioxide on Metallic Copper Surfaces. *Energ. Environ. Sci.* **2012,** *5* (5), 7050-7059, DOI: 10.1039/c2ee21234j.

(21) Li, C. W.; Kanan, M. W. CO_2 Reduction at Low Overpotential on Cu Electrodes Resulting from the Reduction of Thick Cu_2O Films. *J. Am. Chem. Soc.* **2012,** *134* (17), 7231-7234, DOI: 10.1021/ja3010978.

(22) Reske, R.; Mistry, H.; Behafarid, F.; Roldan Cuenya, B.; Strasser, P. Particle Size Effects in the Catalytic Electroreduction of CO_2 on Cu Nanoparticles. *J. Am. Chem. Soc.* **2014,** *136* (19), 6978-6986, DOI: 10.1021/ja500328k.

(23) Loiudice, A.; Lobaccaro, P.; Kamali, E. A.; Thao, T.; Huang, B. H.; Ager, J. W.; Buonsanti, R. Tailoring Copper Nanocrystals towards C-2 Products in Electrochemical CO_2 Reduction. *Angew. Chem.* **2016,** *55* (19), 5789-5792, DOI: 10.1002/anie.201601582.

(24) Hahn, C.; Hatsukade, T.; Kim, Y.-G.; Vailionis, A.; Baricuatro, J. H.; Higgins, D. C.; Nitopi, S. A.; Soriaga, M. P.; Jaramillo, T. F. Engineering Cu Surfaces for the Electrocatalytic Conversion of CO_2: Controlling Selectivity Toward Oxygenates and Hydrocarbons. *Proc Natl Acad Sci U S A* **2017,** *114* (23), 5918-5923, DOI: 10.1073/pnas.1618935114.

(25) Ma, S.; Sadakiyo, M.; Heima, M.; Luo, R.; Haasch, R. T.; Gold, J. I.; Yamauchi, M.; Kenis, P. J. A. Electroreduction of Carbon Dioxide to Hydrocarbons Using Bimetallic Cu-Pd Catalysts with Different Mixing Patterns. *J. Am. Chem. Soc.* **2017,** *139* (1), 47-50, DOI: 10.1021/jacs.6b10740.

(26) Jiang, K.; Sandberg, R. B.; Akey, A. J.; Liu, X. Y.; Bell, D. C.; Norskov, J. K.; Chan, K. R.; Wang, H. T. Metal Ion Cycling of Cu Foil for Selective C-C Coupling in Electrochemical CO_2 Reduction. *Nat. Catal.* **2018,** *1* (2), 111-119, DOI: 10.1038/s41929-017-0009-x.

(27) Taylor, A. D.; Kim, E. Y.; Humes, V. P.; Kizuka, J.; Thompson, L. T. Inkjet Printing of Carbon Supported Platinum 3-D Catalyst Layers for Use in Fuel Cells. *J. Power Sources* **2007,** *171* (1), 101-106, DOI: 10.1016/j.jpowsour.2007.01.024.

(28) Jhong, H. R.; Brushett, F. R.; Kenis, P. J. A. The Effects of Catalyst Layer Deposition Methodology on Electrode Performance. *Adv Energy Mater* **2013,** *3* (5), 589-599, DOI: 10.1002/aenm.201200759.

(29) Wang, Z. Q.; Nagao, Y. Effects of Nafion Impregnation using Inkjet Printing for Membrane Electrode Assemblies in Polymer Electrolyte Membrane Fuel Cells. *Electrochim. Acta* **2014,** *129*, 343-347, DOI: 10.1016/j.electacta.2014.02.133.

(30) Zhao, Y.; Deng, Q. R.; Guo, R. X.; Wu, Z. H.; Li, Y. K.; Duan, Y. Y.; Shen, Y. L.; Zhang, W.; Shao, G. S. Sputtered Ga-Doped SnO_x Electron Transport Layer for Large-Area All-Inorganic Perovskite Solar Cells. *ACS Appl. Mater. Interfaces* **2020,** *12* (49), 54904-54915, DOI: 10.1021/acsami.0c19540.

(31) Kukla, R. Magnetron Sputtering on Large Scale Substrates: An Overview on the State of the Art. *Surf. Coat. Tech.* **1997,** *93* (1), 1-6, DOI: https://doi.org/10.1016/S0257-8972(97)00018-2.

(32) Jankowski, A.; McKernan, M.; Chesser, J. The Use of Magnetron Arrays for Depositing Large-Area Oxide Coatings. *Surf. Coat. Tech.* **2000,** *133-134*, 602-605, DOI: https://doi.org/10.1016/S0257-8972(00)00903-8.

(33) Barranco, A.; Borras, A.; Gonzalez-Elipe, A. R.; Palmero, A. Perspectives on Oblique Angle Deposition of Thin Films: From Fundamentals to Devices. *Prog. Mater. Sci.* **2016,** *76*, 59-153, DOI: https://doi.org/10.1016/j.pmatsci.2015.06.003.

(34) Bakkali, H.; Blanco, E.; Dominguez, M.; de la Mora, M. B.; Sanchez-Ake, C.; Villagran-Muniz, M.; Schmool, D. S.; Berini, B.; Lofland, S. E. The Effect of Oblique-Angle Sputtering on Large Area Deposition: A Unidirectional Ultrathin Au Plasmonic Film Growth Design. *Nanotechnology* **2020,** *31* (44), 445701, DOI: 10.1088/1361-6528/aba65b.

(35) Zhou, Y.; Che, F.; Liu, M.; Zou, C.; Liang, Z.; De Luna, P.; Yuan, H.; Li, J.; Wang, Z.; Xie, H.; Li, H.; Chen, P.; Bladt, E.; Quintero-Bermudez, R.; Sham, T. K.; Bals, S.; Hofkens, J.; Sinton, D.; Chen, G.; Sargent, E. H. Dopant-Induced Electron Localization Drives CO_2 Reduction to C2 Hydrocarbons. *Nat Chem* **2018,** *10* (9), 974-980, DOI: 10.1038/s41557-018-0092-x.

(36) Zhong, M.; Tran, K.; Min, Y. M.; Wang, C. H.; Wang, Z. Y.; Dinh, C. T.; De Luna, P.; Yu, Z. Q.; Rasouli, A. S.; Brodersen, P.; Sun, S.; Voznyy, O.; Tan, C. S.; Askerka, M.; Che, F. L.; Liu, M.; Seifitokaldani, A.; Pang, Y. J.; Lo, S. C.; Ip, A.; Ulissi, Z.; Sargent, E. H. Accelerated Discovery of CO_2 Electrocatalysts using Active Machine Learning. *Nature* **2020,** *581* (7807), 178-183, DOI: 10.1038/s41586-020-2242-8.

(37) Merlo, A.; Leonard, G. Magnetron Sputtering vs. Electrodeposition for Hard Chrome Coatings: A Comparison of Environmental and Economic Performances. *Materials* **2021,** *14* (14), DOI: 10.3390/ma14143823.

(38) Wang, Y.; Nastasi, M. *Handbook of Modern Ion Beam Materials Analysis*, 2010.

(39) Doolittle, L. R. Algorithms for the Rapid Simulation of Rutherford Backscattering Spectra. *Nucl Instrum Meth B* **1985,** *9* (3), 344-351.

(40) Iijima, J.; Lim, J. W.; Hong, S. H.; Suzuki, S.; Mimura, K.; Isshiki, A. Native oxidation of ultra high purity Cu bulk and thin films. *Appl Surf Sci* **2006,** *253* (5), 2825-2829, DOI: 10.1016/j.apsusc.2006.05.063.

(41) Yokomaku, H.; Satoh, W.; Fukuda, J.; Suzuki, H. Electrowetting on Gold Electrodes with Microscopic Three-Dimensional Structures for Microfluidic Devices. *J Appl Phys* **2008,** *104* (6), DOI: 10.1063/1.2976358.

(42) Xue, Y. H.; Markmann, J.; Duan, H. L.; Weissmuller, J.; Huber, P. Switchable Imbibition in Nanoporous Gold. *Nat Commun* **2014,** *5*.

(43) Chai, L.; Klein, J. Large Area, Molecularly Smooth (0.2 nm rms) Gold Films for Surface Forces and Other Studies. *Langmuir* **2007,** *23* (14), 7777-7783, DOI: 10.1021/la063738o.

(44) Tang, W.; Peterson, A. A.; Varela, A. S.; Jovanov, Z. P.; Bech, L.; Durand, W. J.; Dahl, S.; Norskov, J. K.; Chorkendorff, I. The Importance of Surface Morphology in Controlling the Selectivity of Polycrystalline Copper for CO_2 Electroreduction. *Phys. Chem. Chem. Phys.* **2012,** *14* (1), 76-81, DOI: 10.1039/C1CP22700A.

(45) Lomax, D. J.; Kant, P.; Williams, A. T.; Patten, H. V.; Zou, Y.; Juel, A.; Dryfe, R. A. W. Ultra-Low Voltage Electrowetting using Graphite Surfaces. *Soft Matter* **2016,** *12* (42), 8798-8804, DOI: 10.1039/C6SM01565D.

(46) Wang, L.; Nitopi, S.; Wong, A. B.; Snider, J. L.; Nielander, A. C.; Morales-Guio, C. G.; Orazov, M.; Higgins, D. C.; Hahn, C.; Jaramillo, T. F. Electrochemically Converting Carbon Monoxide to Liquid Fuels by Directing Selectivity with Electrode Surface Area. *Nat. Catal.* **2019,** *2* (8), 702-708, DOI: 10.1038/s41929-019-0301-z.

(47) Martín, A. J.; Larrazábal, G. O.; Pérez-Ramírez, J. Towards Sustainable Fuels and Chemicals through the Electrochemical Reduction of CO_2: Lessons from Water Electrolysis. *Green Chem.* **2015,** *17* (12), 5114-5130, DOI: 10.1039/C5GC01893E.

(48) Corral, D.; Feaster, J. T.; Sobhani, S.; DeOtte, J. R.; Lee, D. U.; Wong, A. A.; Hamilton, J.; Beck, V. A.; Sarkar, A.; Hahn, C.; Jaramillo, T. F.; Baker, S. E.; Duoss, E. B. Advanced Manufacturing for Electrosynthesis of Fuels and Chemicals from CO_2. *Energ Environ Sci* **2021,** *14* (5), 3064-3074, DOI: 10.1039/d0ee03679j.

TOC:

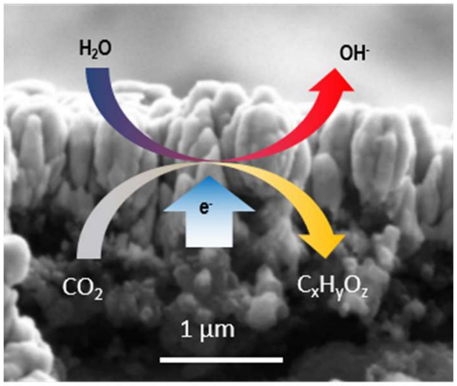

H2O
OH-
e-
CO2
CxHyOz
1 µm

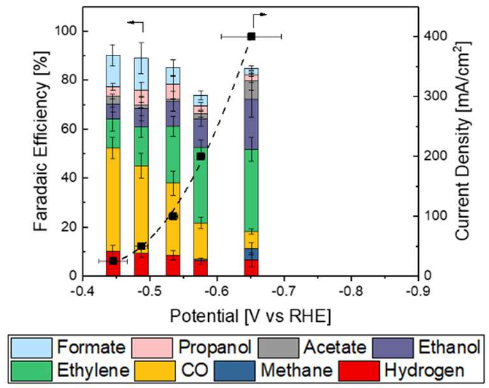

Faradaic Efficiency [%]
Current Density [mA/cm2]
Potential [V vs RHE]
Formate
Propanol
Acetate
Ethanol
Ethylene
CO
Methane
Hydrogen